Mon. Not. R. Astron. Soc. **369,** 1667–1676 (2006) doi:10.1111/j.1365-2966.2006.10284.x

X-ray gas in the galaxy cluster Abell 2029: conformal gravity versus dark matter

Keith Horne★
SUPA, St Andrews University, Physics and Astronomy, North Haugh, St Andrews KY16 9SS

Accepted 2006 March 3. Received 2005 November 21

ABSTRACT

Conformal gravity has a weak-field limit that augments the Newtonian potential $-GM/R$ by a linear potential $\gamma c^2 R/2$. Mannheim has shown that an appropriate choice of γ enables a satisfying fit to the flat rotation curves of large spiral galaxies and simultaneously to the rising rotation curves of low surface brightness galaxies, without invoking dark matter. Here, we extend to larger scales the comparison of Newtonian and conformal gravity by analysis of X-ray gas in the Abell 2029 galaxy cluster. The Newtonian analysis yields a mass profile rising roughly as $M \propto R^2$ from $10^{10}\,\mathrm{M}_\odot$ at 2 kpc to $10^{14}\,\mathrm{M}_\odot$ at 200 kpc, and this can be interpreted as the profile of an extensive dark matter halo that dominates the cluster potential. In conformal gravity, the potential is non-uniform inside a spherical shell, so that both interior and exterior mass distributions must be taken into account. We derive the conformal gravity potential both inside and outside a spherical shell, enabling the evaluation of potentials for spherically symmetric mass distributions. A conformal gravity analysis of X-ray gas in Abell 2029 then yields a total mass profile that rises from $10^{10}\,\mathrm{M}_\odot$ at 2 kpc to $1.4 \times 10^{12}\,\mathrm{M}_\odot$ at 30 kpc, and then remains roughly constant out to 300 kpc. With this mass profile, conformal gravity is able to bind the X-ray gas with no need for dark matter. However, integrating the X-ray gas density profile gives a baryon mass of $10^{13}\,\mathrm{M}_\odot$ inside 200 kpc, nearly 10 times more than what is required to hold the hot gas in hydrostatic equilibrium. This discrepancy may rule out conformal gravity unless there is a significant breakdown of hydrostatic equilibrium in the outskirts of the potential well. The required velocities, $V \sim 2000\,\mathrm{km\,s^{-1}}$, may be observable via Doppler profiles in high-resolution X-ray spectroscopy. It is also possible that the mass distribution outside the cluster significantly reduces conformal gravity in the cluster outskirts. Our approximate treatment of this effect suggests that it is negligible, but a more sophisticated analysis might yield a different conclusion.

Key words: galaxies: clusters: individual: Abell 2029 – cosmology: theory – dark matter – X-rays: galaxies: clusters.

1 INTRODUCTION

Rich clusters of galaxies are generally filled with hot gas that appears to be in virial equilibrium. X-ray observations of thermal emission from the hot gas have recently achieved sufficient spatial and spectral resolution to establish reliably the run of density, temperature and abundances with radius. Measurements of the hot gas pressure and density profile then provide the basis for inferring the total mass profile of the gravitational well that confines the hot gas. Assuming that the hot gas is in hydrostatic equilibrium,

$$\frac{\mathrm{d}P}{\mathrm{d}R} = -\rho\frac{\mathrm{d}\Phi}{\mathrm{d}R} = -\rho g, \tag{1}$$

the gas pressure $P(R)$ and density $\rho(R)$ provide a probe of the gravitational potential Φ and the corresponding acceleration g. For Newtonian gravity, the potential and acceleration are

$$\Phi_\mathrm{N} = -\frac{G\,M}{R} \tag{2}$$

and

$$g_\mathrm{N} = \frac{\mathrm{d}\Phi_\mathrm{N}}{\mathrm{d}\,R} = \frac{G\,M}{R^2}. \tag{3}$$

The mass profile needed to confine and maintain the hydrostatically supported X-ray gas is then

$$M_\mathrm{N} = -\frac{R^2}{G\rho}\frac{\mathrm{d}P}{\mathrm{d}R} = \frac{R\,c_\mathrm{s}^2}{G}\left[-\frac{\mathrm{d}\ln P}{\mathrm{d}\ln R}\right], \tag{4}$$

★E-mail: kdh1@st-and.ac.uk

where the sound speed for a perfect gas equation of state is

$$c_s^2 = \frac{P}{\rho} = \frac{k\,T}{\mu\,m_H}, \tag{5}$$

with μ mean molecular weight and m_H the mass of a hydrogen atom.

Fits to observed X-ray spectra provide estimates for $T(R)$, $\rho(R)$ and abundances [hence $\mu(R)$], yielding $c_s(R)$ and $P(R)$, as functions of distance R from the cluster centre. This enables estimates of the mass profile, $M(R)$, via equation (4). Differentiation of $P(R)$ makes the result unstable to measurement errors, however, so the usual procedure is to fit a smooth function to the observed $P(R)$, and differentiate that smooth function when evaluating $M(R)$. The observations typically show that $T(R)$ is a weak function of R, while $\rho(R)$ decreases rapidly with R. Thus $P(R)$ decreases with R, and the resulting $M(R)$ from equation (4) is then positive. If $T(R)$ and $P(R)$ are asymptotically power-law functions, the factor R in the numerator of equation (4) usually makes $M(R)$ increase steeply with R. To make $M(R)$ decrease T would need to drop off faster than $1/R$. Thus the Newtonian analysis usually yields $M(R)$ rising with R rather than reaching a constant value.

In the mass budget for known baryons, stars typically dominate in the core and hot gas in the outskirts of the cluster. The stellar baryons can usually be made to match the total mass profile in the inner regions by adopting a plausible mass-to-light ratio for the stars. In the outer regions of the cluster, where the hot gas dominates the baryon density, Newtonian gravity from known baryonic sources appears to be insufficient by factors of the order of 10, and this is taken as evidence that the cluster potential in these outer regions is dominated by dark matter.

In this paper, we consider whether Mannheim's conformal gravity theory (Mannheim & Kazanas 1989; Mannheim 1993, 1997, 2001, 2006) can account for the confinement of hot gas in galaxy clusters without recourse to dark matter. (Mannheim 1996) showed that the velocity dispersion in the virialized core of the Coma cluster could be accounted for, and raised some questions about the time-scale to reach virial equilibrium in the outskirts of the cluster. In Section 2 we briefly summarize relevant features of conformal gravity, including its success in fitting observations of spiral galaxy rotation curves. We then derive (with help from Appendix A) the required modifications to equation (4). In Section 3, we apply the analysis to *Chandra* observations of the hot gas in the rich galaxy cluster Abell 2029. We find that Netwonian gravity provides insufficient inward acceleration while conformal gravity provides more than enough inward acceleration to hold the hot gas in hydrostatic equilibrium. In Section 4, we discuss the problem of too much conformal gravity in the cluster outskirts, and several possibilities for reducing it. Section 5 summarizes our conclusions. Appendix A develops conformal gravity formulae for the potential, gravity and rotation curve for a spherical shell, for a Hernquist mass profile, and for a uniform density sphere. We show also that long-range shielding of the linear potential may occur if overdense regions are cancelled by surrounding voids of equivalent mass.

2 CONFORMAL GRAVITY

Conformal gravity is a covariant metric theory of gravity derived from the principle of local conformal symmetry. Invariance to local isotropic stretching of the space–time fabric

$$g_{\mu\nu}(x) \rightarrow \Omega^2(x) g_{\mu\nu}(x), \tag{6}$$

where $g_{\mu\nu}(x)$ is the metric tensor, leads to a unique scalar action

$$I_W = -\alpha \int \sqrt{-g}\; \mathrm{d}^4x\; C_{\mu\nu\lambda\kappa}\, C^{\mu\nu\lambda\kappa}, \tag{7}$$

where $C_{\mu\nu\lambda\kappa}$ is the conformal Weyl tensor (Weyl 1918) and α is a dimensionless scalar. As in general relativity, test particles follow geodesic trajectories in curved space–time. However, Einstein's second-order field equations are replaced in conformal gravity by fourth-order field equations derived from the Weyl action.

An exact solution for the vacuum exterior to a static point source is given (Mannheim & Kazanas 1989) by the line element

$$\mathrm{d}s^2 = -B(r)c^2\mathrm{d}t^2 + \frac{\mathrm{d}r^2}{B(r)} + r^2(\mathrm{d}\theta^2 + \sin^2\theta\,\mathrm{d}\phi^2), \tag{8}$$

with time coordinate t, spherical polar spatial coordinates r, θ, ϕ, and

$$B(r) = 1 - 3\beta\gamma - \frac{\beta(2-3\beta\gamma)}{r} + \gamma r - \kappa r^2, \tag{9}$$

where β, γ and κ are integration constants. Solutions including charge and spin are also available (Mannheim & Kazanas 1991). Identifying $B(r) = 1 + 2\Phi/c^2$, the effective gravitational potential is

$$\frac{\Phi}{c^2} = -\frac{\beta\,(1-3\beta\gamma/2)}{r} - \frac{3\,\beta\,\gamma}{2} + \frac{\gamma\,r}{2} - \frac{\kappa r^2}{2}. \tag{10}$$

Consistency with Solar system dynamics requires $B(r) \rightarrow 1 - 2GM/c^2r$ for $M \sim \mathrm{M}_\odot$ and $r < 10^{15}$ cm. This is obtained if $\gamma \ll 10^{-15}\,\mathrm{cm}^{-1}$ and

$$\beta = \frac{G\,M}{c^2} = 1.48 \times 10^5 \left(\frac{M}{\mathrm{M}_\odot}\right) \mathrm{cm}. \tag{11}$$

The solution connects smoothly on to a Schwarzschild metric for $r \ll r_1$, and a Robertson–Walker metric with 3-space curvature $K = -\kappa - \gamma^2/4$ for $r \gg r_1$, where $r_1 = (2\beta/\gamma)$ (Mannheim & Kazanas 1989).

2.1 Galaxy rotation curves

The fourth-order field equations of conformal gravity lead in the weak-field limit to a fourth-order Poisson equation,

$$\nabla^4\Phi = -4\pi G\rho, \tag{12}$$

with the vacuum solution

$$\frac{\Phi}{c^2} = -\frac{\beta}{r} + \frac{\gamma\,r}{2} - \frac{\kappa\,r^2}{2}. \tag{13}$$

The quadratic term, important on cosmological scales, is hereafter neglected. The linear potential term augments Newtonian gravity with an additional r-independent inward acceleration $\gamma c^2/2$. This term enables successful fits to spiral galaxy rotation curves (Mannheim 1993, 1997) provided

$$\gamma = \gamma_0 + \left(\frac{M}{\mathrm{M}_\odot}\right)\gamma^\star, \tag{14}$$

with $\gamma_0 = 3.06 \times 10^{-30}\,\mathrm{cm}^{-1}$ and $\gamma^\star = 5.42 \times 10^{-41}\,\mathrm{cm}^{-1}$.

In this paper, we adopt the equivalent parametrization

$$\Phi = \Phi_N + \Phi_M = -\frac{G\,M}{R} + \frac{G\,M_0}{R_0}\left(\frac{M}{M_0} + 1\right)\frac{R}{R_0}, \tag{15}$$

where the values of γ_0 and $\gamma^\star$ above translate to $R_0 \approx 24$ kpc and $M_0 \approx 5.6 \times 10^{10}\,\mathrm{M}_\odot$. The first term is the Newtonian

potential, and the additional non-Newtonian terms are the Mannheim potential.

Strictly speaking, this is the Newton–Mannheim potential for empty space around a point mass M. For extended mass distributions, we assume for the moment that we can replace M by the enclosed mass $M(R)$. For a spherically symmetric mass distribution this approximation is exact for the Newtonian potential, but there are corrections to the Mannheim potential. These we derive in Appendix A and take into account in the analysis of cluster mass profiles to follow below.

The inward gravitational acceleration arising from the Newton–Mannheim potential is

$$g = \frac{\mathrm{d}\Phi}{\mathrm{d}R} = \frac{G\,M}{R^2} + g_0\left(\frac{M}{M_0} + 1\right), \tag{16}$$

where

$$g_0 = \left(\frac{G\,M_0}{R_0^2}\right) \approx 1.4 \times 10^{-9}\ \mathrm{cm\,s^{-2}}. \tag{17}$$

The corresponding circular orbit velocity is

$$V^2 = g\,R = \frac{G\,M}{R} + V_0^2\left(\frac{M}{M_0} + 1\right)\frac{R}{R_0}, \tag{18}$$

where

$$V_0 = \left(\frac{G\,M_0}{R_0}\right)^{1/2} \approx 100\ \mathrm{km\,s^{-1}}. \tag{19}$$

The Mannheim terms affect dynamics in the outskirts of galaxies. The transition between the interior Newtonian and exterior Mannheim regimes occurs at

$$R_\mathrm{M} \approx R_0\left(\frac{M}{M + M_0}\right). \tag{20}$$

For large galaxies, $M > M_0$, the Mannheim radius is $R_\mathrm{M} \approx R_0$, independent of mass. As the Kepler velocity falls, the Mannheim velocity rises, giving a flat rotation curve with $V \sim V_0\sqrt{2M/M_0}$ over a wide range in R around R_M before rising as $V \sim V_0\sqrt{RM/R_0M_0}$. For smaller galaxies, $M < M_0$, the Newtonian region shrinks to $R < R_\mathrm{M} \approx R_0M/M_0$, outside which the velocity profile is $V \approx V_0\sqrt{R/R_0}$, independent of mass. This accounts for the rising rotation curves of low surface brightness galaxies that are often interpreted as dark matter dominated.

2.2 Galaxy cluster mass profiles

For galaxy clusters, we have $M > M_0$, and we therefore expect the Mannheim terms to be important for $R > R_0 \approx 24$ kpc. The hydrostatic equilibrium equation is now

$$g = -\frac{1}{\rho}\frac{\mathrm{d}P}{\mathrm{d}R} = \frac{G\,M}{R^2} + g_0\left(\frac{M}{M_0} + 1\right) + \Delta g. \tag{21}$$

Here, we denote by Δg the correction that accounts for the effect of the extended mass distribution. The extended source corrections are derived in Appendix A. These arise because the Mannheim effects from a spherical shell differ from those from a point source of equivalent mass. For completeness, we note here that

$$\frac{\Delta g(R)}{g_0} = \frac{2}{3}\int_{r>R}\frac{R}{r}\frac{\mathrm{d}M}{M_0} - \frac{1}{3}\int_{r<R}\left(\frac{r}{R}\right)^2\frac{\mathrm{d}M}{M_0}, \tag{22}$$

where $\mathrm{d}\,M = 4\pi r^2\rho\,\mathrm{d}r$. Thus external shells of material, $r > R$, enhance the inward gravity, and internal shells, $r < R$, are a bit weaker than the equivalent point mass.

If M_N is the mass profile derived by Newtonian dynamics, given by equation (4), then the mass profile obtained including the Mannheim terms is

$$M = \frac{M_\mathrm{N} - M_0\,(R/R_0)^2 - \Delta M}{1 + (R/R_0)^2}, \tag{23}$$

where $\Delta M = R^2\Delta g/G$. Note that because Δg depends on the mass profile, $M(R)$, we must iterate equation (23) to obtain a self-consistent solution.

The Mannheim corrections tend to reduce the mass, and thus offer the hope that a finite total mass can be achieved. Note that for $R > R_0$ the denominator of equation (23) is an increasing function of R. If the numerator fails to increase at least as fast, the ratio can give M decreasing with R. This unphysical result could either rule out the conformal gravity theory, or else indicate a breakdown of the assumption of hydrostatic equilibrium.

3 APPLICATION TO ABELL 2029

To illustrate the difference between a Newtonian and conformal gravity analysis of X-ray gas in galaxy cluster potentials, we consider the Abell 2029 galaxy cluster. *Chandra* observations of the X-ray gas are described in (Lewis, Stocke & Buote 2002), where the radial profiles of gas temperature and Fe abundance are evaluated from spectral fits to spatially resolved X-ray spectra. A mass profile dominated by dark matter in the outer regions is derived from the Newtonian analysis presented in (Lewis, Buote & Stocke 2003).

We have repeated the analysis of (Lewis et al. 2003) from the measured temperature and density versus angular distance. We adopt $H_0 = 70\ \mathrm{km\,s^{-1}\,Mpc^{-1}}$, redshift $z = 0.0767$, luminosity distance $d = cz/H_0 = 328$ Mpc, and angular scale 1.59 arcsec pc^{-1}. Fig. 1 summarizes the results of our analysis, showing the radial profile of the temperature (a), density (b), sound speed (c) and pressure (d) in the hot gas, and the derived radial profiles for gravity (e, f) and enclosed mass (g, h), assuming hydrostatic equilibrium, for both Newtonian (e, g) and conformal gravity (f, h).

The temperature $T(R)$ rises from 3×10^7 K at 2 kpc to 10^8 K at 200 kpc, while the gas density $\rho(R)$ drops by a factor of 30 and the pressure $P(R)$ by a factor of 10 over the same range. For the sound speed c_s we assume a mean molecular weight $\mu = 0.6$, and we plot for comparison in Fig. 1(c) the observed velocity dispersion σ_V of the starlight in the central cD galaxy (Dressler 1979), and of the cluster galaxies (Dressler 1981; Dale & Uson 2000). From the density and pressure profiles, we use equation (1) to derive the inward acceleration $g(R)$ that is required to support the hot gas in hydrostatic equilibrium (Figs 1e and f). Large error bars in the inner regions stem from the numerical derivative of the pressure profile, mainly from uncertainties in the gas temperature measurements. The gravity profile is almost flat, varying by less than a factor of 3 between 2 and 300 kpc. The derived gravity, $g \approx 2$–$6 \times 10^{-8}\ \mathrm{cm\,s^{-2}}$, is just above the acceleration threshold $a_0 \approx 1.2 \times 10^{-8}\ \mathrm{cm\,s^{-2}}$ in the modified Newtonian dynamics (MOND) theory (Milgrom 1983; Sanders & McGaugh 2002). We therefore expect that a MOND analysis of A2029 would give results similar to those of the Newtonian analysis, with a slightly higher gravity and lower total mass, but still insufficient baryons to generate the gravity required to bind the hot gas (Sanders 2003).

In the lower panels of Fig. 1, thick lines with error bars show the gravity and total mass profile derived from the hot gas thermal equilibrium equation, for Newtonian (Fig. 1g) and conformal gravity

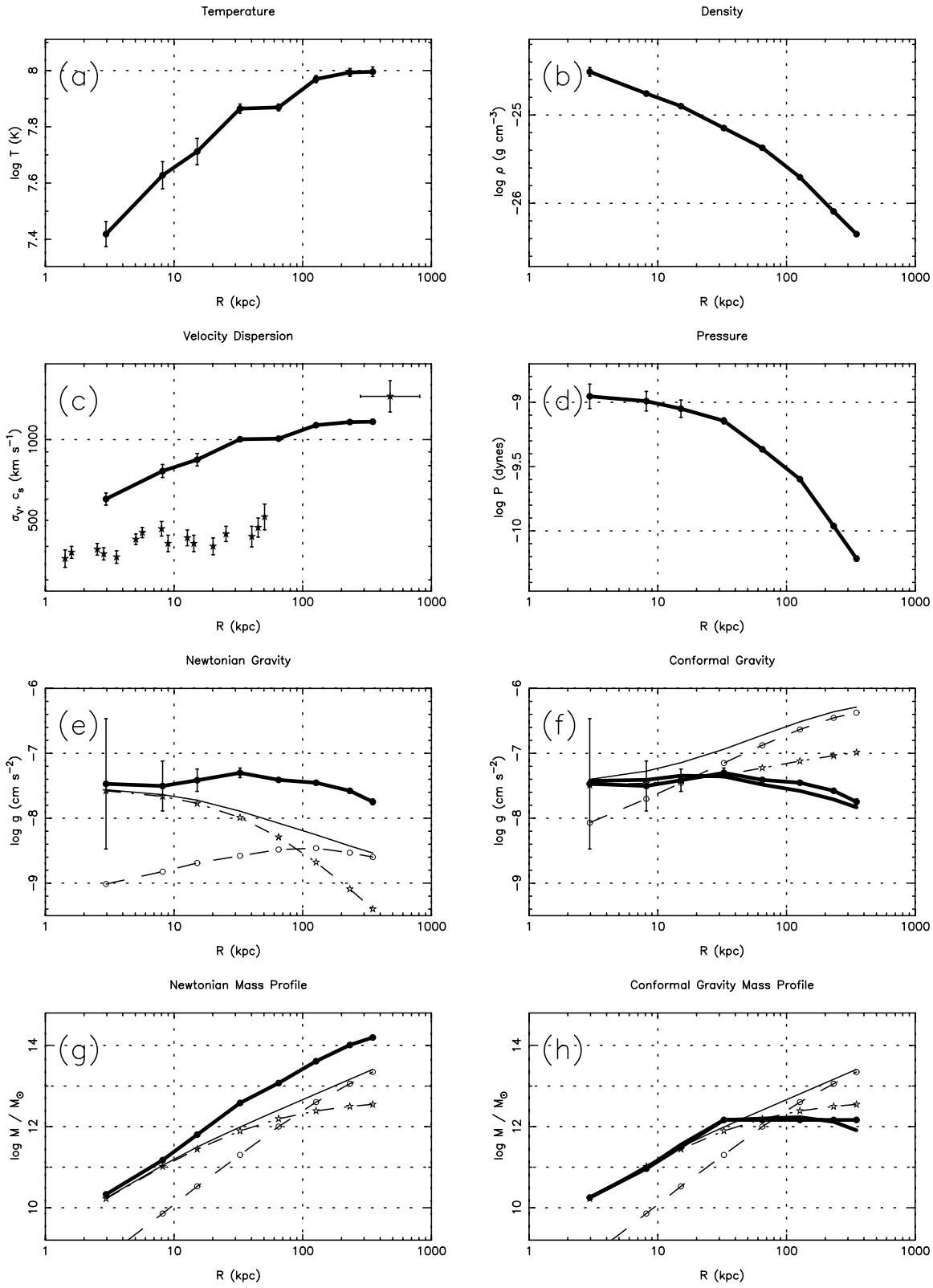

Figure 1. Top two rows: analysis of *Chandra* observations of X-ray spectra emitted by hot gas in the galaxy cluster Abell 2029 yields estimates for the temperature (a), density (b), sound speed (c) and pressure (d) versus radius, from (Lewis et al. 2003). In (c) the observed velocity dispersion σ_V of starlight from the central CD galaxy (Dressler 1979) is is somewhat below the hot gas sound speed c_s, while that of the cluster galaxies (Dressler 1981; Dale & Uson 2000) is somewhat above. Bottom two rows: thick lines give the inward gravity (e, f) required to maintain the hot gas in hydrostatic equilibrium, and the resulting enclosed total mass profiles (g, h), for both Newtonian (e, g) and conformal gravity (f, h). For comparison, thin curves give gravity and mass profiles for the baryons, divided into contributions from stars and hot gas, marked with stars and open circles, respectively. Newtonian gravity is insufficient while conformal gravity is more than sufficient to bind the hot gas in the outskirts of the cluster.

(Fig. 1h). For comparison, the thin dashed curves (marked with stars and open symbols) show the gravity and mass profiles for the stars and hot gas, and the unmarked thin curve is the total mass of known baryons (stars plus hot gas). For the gas we integrate the gas density profile derived from the *Chandra* spectra (Lewis et al. 2003). For the stars we adopt a Hernquist model (Section A5) with characteristic radius $A = 46\,\mathrm{kpc}$ and total mass $M = 4.5 \times 10^{12}\,\mathrm{M}_\odot$. This matches the stellar mass profile derived by (Lewis et al. 2003) from the photometry of (Uson, Boughn & Kuhn 1991) for a mass-to-light ratio $M_\star/L_V \approx 12$.

In the heart of the cluster, $R < 20\,\mathrm{kpc}$, Newtonian gravity of the stars dominates the dynamics. The adopted stellar mass profile is in good agreement with what is required to hold the hot gas in hydrostatic equilibrium. The star density falls more rapidly than the gas density, so that hot gas dominates the baryon budget in the cluster outskirts. At 200 kpc, Newtonian gravity from interior baryons falls short by a factor of 10 of what is required to confine the hot gas. (Lewis et al. 2003) find a mass-to-light ratio rising from ∼12 inside 20 kpc to above ∼100 outside 200 kpc, and our Newtonian analysis broadly confirms their findings.

Total enclosed mass profiles derived for Newtonian and conformal gravity are shown in the bottom panel of Fig. 1. With Newtonian gravity the total mass profile rises from $10^{10}\,\mathrm{M}_\odot$ at $R \approx 2\,\mathrm{kpc}$ to $10^{14}\,\mathrm{M}_\odot$ at $R \approx 200\,\mathrm{kpc}$. This is a factor of 10 higher than the gas mass, obtained by integrating the gas density profile, which rises from from $10^{8}\,\mathrm{M}_\odot$ at $R \approx 2\,\mathrm{kpc}$ to $10^{13}\,\mathrm{M}_\odot$ at $R \approx 200\,\mathrm{kpc}$. Rising mass profiles such as this are currently interpreted as evidence for an extensive dark matter halo.

Our conformal gravity analysis gives a total mass profile that rises from $10^{10}\,\mathrm{M}_\odot$ at 2 kpc to $1.4 \times 10^{12}\,\mathrm{M}_\odot$ at 30 kpc, and then remains flat out to 300 kpc. We present two solutions, shown as the two thick lines in Figs 1(f) and (h). One satisfies the hydrostatic equilibrium equation (21) exactly, but the numerical integration of equation (23) gives $M(R)$ decreasing slightly in the outer regions. For the second solution we force the density to be positive when integrating equation (23), so that $M(R)$ cannot decrease with R, and this solution does not quite satisfy equation (21), having a slightly higher gravity inside and lower gravity outside 30 kpc. The agreement between the two is satisfactory. Within the uncertainties of the analysis, the total mass reaches an asymptotic value, rather than continuing to rise indefinitely.

4 TOO MUCH CONFORMAL GRAVITY

We have found that the radial structure of the X-ray gas in A2029 requires a gravitational acceleration $\log g \approx -7.4$, approximately independent of radius. With Newtonian gravity, this requires a total mass increasing roughly as $M \propto R^2$, rising to $10^{14}\,\mathrm{M}_\odot$ at 200 kpc where it exceeds by a factor of 10 the enclosed mass of stars and gas. The conventional interpretation is that Newtonian gravity requires this cluster, and others like it, to reside within an extensive halo of dark matter. In A2029, the inferred dark matter density falls off roughly as $\rho \propto R^{-1}$.

With conformal gravity, a total mass $M \approx 1.4 \times 10^{12}\,\mathrm{M}_\odot$ ($\approx 25\,M_0$) within about 30 kpc ($1.1R_0$) suffices to account for the radial structure of the X-ray gas in A2029. Gas at larger radii is confined by the inward gravitational acceleration $g_0\,M/M_0$ arising from the source-generated Mannheim potential of the interior baryons. We conclude that conformal gravity does not require dark matter to confine the X-ray gas in A2029, and by extension in other similar galaxy clusters.

However, the apparent success of conformal gravity in eliminating the need for dark matter is somewhat marred by the fact that the gas mass rises to $10^{13}\,\mathrm{M}_\odot$ at 200 kpc, a factor of 10 higher than the required total mass. Thus conformal gravity in our analysis generates an inward acceleration that is more than sufficient to hold the gas in hydrostatic equilibrium.

What may have gone wrong? We discuss briefly several possibilities that we have considered.

(1) Does hydrostatic equilibrium break down? Could the gas be rotating, falling in, flowing out, or supported by supersonic turbulence? The X-ray surface brightness in A2029 is quite smooth (Lewis et al. 2002), indicating that the gas is relatively relaxed and not obviously disturbed. The central cD galaxy is clearly flattened and rotating, with a 2:1 axis ratio (Uson et al. 1991), a velocity dispersion of 400–500 km s^{-1} (Fig. 1c) and a projected rotation velocity of 200 km s^{-1} (Dressler 1979). The X-ray emission is also flattened, with a 1.4:1 axis ratio (Lewis et al. 2002), so there is some evidence for rotational support, or at least an anisotropic potential well. The X-ray gas sound speed is 600–1400 km s^{-1} (Fig. 1c), and comparable bulk velocities would be required to significantly affect the gas dynamics. The cluster galaxies have a velocity dispersion of ≈1450 km s^{-1} (Dressler 1981; Oegerle, Hill & Fitchett 1995; Dale & Uson 2000), and these may help to stir up the hot gas. A velocity $V \sim \sqrt{2Rg} \approx 2000\,\mathrm{km\,s^{-1}}$ could loft gas to $R \approx 200\,\mathrm{kpc}$ against the gravity $g \approx g_0 M/M_0 \approx 3 \times 10^{-8}\,\mathrm{cm\,s^{-2}}$. Measurements of Doppler shifts or broadening of X-ray spectral lines emitted by the hot gas could test the hypothesis that bulk motions augment thermal gas pressure support.

(2) Our analysis adopted a mean molecular weight of 0.6, neglecting the observed radial gradient of Fe abundance, which decreases from twice to half solar between 2 and 200 kpc (Lewis et al. 2002). Higher metal abundances in the core will supply fewer electrons per baryon, increasing the mean molecular weight and lowering the sound speed there, but this effect should not be large enough to affect our analysis significantly.

(3) The derived total mass profile in Fig. 1(h) is close to the baryon mass profile for the stars only, omitting the gas. If somehow the Mannheim linear potential were generated by baryons (or other sources) associated with the stars, but not by those associated with the hot gas, that would give a more satisfying fit. This is probably a logical possibility, since the strength of the source-generated linear potential depends on the internal structure of the sources. Heavy nuclei could have a stronger linear potential per baryon than lighter nuclei, for example. However, we regard this as a rather inelegant solution.

(4) In conformal gravity, exterior matter can affect the interior dynamics. Because the linear potential increases without bound, sources well outside the cluster may not be negligible. In particular, Section A6 shows that the effective gravity in the outskirts of the cluster could be reduced if the cluster is surrounded by a low-density region. Such a void may be expected if the cluster was assembled by gravitational collapse, collecting matter from a larger region of originally nearly uniform baryon density. The background baryon density is

$$\bar{\rho}_\mathrm{b} = \frac{3\,H_0^2\Omega_\mathrm{b}}{8\pi G}(1+z)^3. \tag{24}$$

Using $H_0 = 70\,\mathrm{km\,s^{-1}\,Mpc^{-1}}$, $\Omega_\mathrm{b} = 0.04$ and $z = 0.0767$ gives $\bar{\rho}_\mathrm{b} \approx 4.6 \times 10^{-31}\,\mathrm{g\,cm^{-3}}$. If the cluster mass M matches the mass

deficit in the surrounding void, the void radius would be

$$R_{\rm void} \approx \left(\frac{3M}{4\pi\bar{\rho}_{\rm b}}\right)^{1/3} = \left(\frac{2GM}{H_0^2\Omega_{\rm b}}\right)^{1/3}\frac{1}{1+z}$$
$$\approx 18\,{\rm Mpc}\left(\frac{M}{10^{13}\,{\rm M}_\odot}\right)^{1/3}\left(\frac{\Omega_{\rm b}}{0.04}\right)^{-1/3}. \quad (25)$$

The outward acceleration produced within the cluster by this external void (see Section A6) is

$$g_{\rm void} \approx g_0\frac{M}{M_0}\frac{R}{R_{\rm void}}$$
$$\approx 2.6\times10^{-9}\,{\rm cm\,s^{-2}}\left(\frac{M}{10^{13}\,{\rm M}_\odot}\right)^{2/3}\left(\frac{R}{200\,{\rm kpc}}\right). \quad (26)$$

This is two orders of magnitude smaller than what would be required to significantly reduce the conformal gravity in the cluster outskirts. In our analysis, we used the results in Section A6 to include the outward acceleration caused by an external void, but this has little effect on the results. However, treating the external mass distribution as a spherical void around the cluster may be too simple to accurately evaluate the order of magnitude of the external effects, so we consider this possibility worthy of further investigation.

(5) We neglected the quadratic term $\kappa\, r^2/2$ in the Mannheim potential (equation 13). This term can generate a repulsive gravity $g = c^2\kappa r/2$, increasing with r, and is normally attributed to effects of the external negatively curved space–time (Mannheim 2001), with $\kappa \sim (H_0/c)^2$. We neglected the quadratic term in this paper because it should be important only on cosmological scales. We could postulate a source-generated contribution to κ, analogous to the splitting of γ into γ_0 and $\gamma^\star$ that was required to fit rotation curves of both low- and high-mass galaxies. Adding a new fitting parameter would not be an economical solution unless analysis of other clusters showed that the same value works for all clusters. Even then, the required term would probably upset the conformal gravity cosmology (Mannheim 2001).

5 SUMMARY AND CONCLUSION

We have shown that conformal gravity is sufficient without dark matter to bind the observed X-ray gas in the rich galaxy cluster Abell 2029. We have used the temperature and density profile derived from *Chandra* observations of X-ray emission from the hot gas in Abell 2029 (Lewis et al. 2002, 2003) to derive the mass profile of the cluster in the context of both Newtonian and conformal gravity. With Newtonian gravity the mass profile rises continuously from $10^{10}\,{\rm M}_\odot$ at 2 kpc to $10^{14}\,{\rm M}_\odot$ at 200 kpc, consistent with the results of (Lewis et al. 2003), requiring a dark matter halo that dominates the potential. With conformal gravity, however, the mass profile rises to to $10^{12}\,{\rm M}_\odot$ at 30 kpc, and is constant thereafter. The source-generated linear potential of conformal gravity provides a potential well deep enough to bind the X-ray gas in Abell 2029 without resorting to dark matter.

However, this promising result is spoiled by the fact that the total mass in stars and gas, mainly in gas, rises to $10^{13}\,{\rm M}_\odot$ at 200 kpc. This exceeds by a factor 10 the mass found from the conformal gravity analysis of the hot gas. Conformal gravity therefore appears to be more than sufficient to bind the X-ray gas. This discrepancy might be due to a violation of the assumption of hydrostatic equilibrium in the X-ray gas. Potentially observable bulk velocities or velocity dispersions, of the order of $2000\,{\rm km\,s^{-1}}$ could test this hypothesis. Alternatively, dynamics in the cluster outskirts might be significantly affected by the external mass distribution. Our rough estimate, allowing for an external void of equal mass to the cluster, suggests that this effect is too small, but more detailed investigation may yield different conclusions.

ACKNOWLEDGMENTS

Thanks go to Aaron Lewis for kindly providing data on the radial structure of the X-ray gas in Abell 2029 that was used in the present analysis, to Philip Mannheim for enthusiasm and tuition on relevant aspects of conformal gravity, and to HongSheng Zhao for comments on the manuscript. This work was partially supported via the award of a PPARC Senior Fellowship at the University of St Andrews, and a Beatrice Tinsley Visiting Professorship at the University of Texas, Austin.

REFERENCES

Dale D. A., Uson J. M., 2000, ApJ, 120, 552
Dressler A., 1979, ApJ, 231, 659
Dressler A., 1981, ApJ, 243, 26
Hernquist L., 1990, ApJ, 356, 359
Lewis A. D., Stocke J. T. Buote D. A., 2002, ApJ, 573, L13
Lewis A. D., Buote D. A., Stocke J. T., 2003, ApJ, 586, 142
Mannheim P. D., 1993, ApJ, 419, 150
Mannheim P. D., 1996, in ASP Conf. Ser. Vol. 88, Clusters, Lensing, and the Future of the Universe. Astron. Soc. Pac., San Francisco, p. 284
Mannheim P. D., 1997, ApJ, 479, 659
Mannheim P. D., 2001, ApJ, 561, 1
Mannheim P. D., 2006, Prog. Part. Nucl. Phys., 56, 340
Mannheim P. D., Kazanas D., 1989, ApJ, 342, 635
Mannheim P. D., Kazanas D., 1991, Phys. Rev. D, 44, 417
Milgrom M., 1983, ApJ, 342, 635
Oegerle W. R., Hill J. M., Fitchett M. J., 1995, AJ, 110, 32
Sanders R. H., 2003, MNRAS, 342, 901
Sanders R. H., McGaugh S. S., 2002, ARA&A, 40, 263
Uson J. M., Boughn S. P., Kuhn J. R., 1991, ApJ, 369, 46
Weyl H., 1918, Math. Zeit., 2, 384

APPENDIX A: SPHERICAL POTENTIALS

A1 Newtonian gravity

Most readers will be familiar with the main properties of the Newtonian potential,

$$\Phi_{\rm N} = -\frac{GM}{R}, \quad (A1)$$

which gives rise to Newton's inverse-square law

$$g_{\rm N} = \frac{{\rm d}\Phi_{\rm N}}{{\rm d}R} = \frac{GM}{R^2}, \quad (A2)$$

and the Keplerian velocity

$$V_{\rm K} = \left(R\frac{{\rm d}\Phi_{\rm N}}{{\rm d}R}\right)^{1/2} = \left(\frac{GM}{R}\right)^{1/2}. \quad (A3)$$

The above results apply to empty space around a point mass M. In the Newtonian case, the generalization to extended spherically symmetric mass distributions $\rho(R)$ is a straightforward replacement of the point mass M by $M(R)$, the mass enclosed within radius R,

$$M(R) = 4\pi\int_0^R r^2\rho(r)\,{\rm d}r. \quad (A4)$$

This is possible because the potential from a spherical shell enclosing the point at radius R is constant, and thus there is no net acceleration from the material at larger radii.

A2 Conformal gravity

In the weak-gravity limit, conformal gravity augments the familiar Newtonian potential with an additional 'Mannheim' potential (Mannheim 1993, 1997)

$$\Phi_M = \left[\frac{\gamma_\star c^2}{2}\left(\frac{M}{\mathrm{M}_\odot}\right) + \frac{\gamma_0\, c^2}{2}\right] R, \tag{A5}$$

The Mannheim potential is proportional to R, and has two parts. The source-generated part, $\gamma_\star c^2 R M/2\,\mathrm{M}_\odot$, scales with mass and is interpreted as arising from the internal structure of elementary particles. The cosmological part, $\gamma_0\, c^2 R/2$, is independent of mass and stems from the curved external space–time in which the object is embedded.

We can write the Newton–Mannheim potential in a dimensionless form,

$$\Phi = V_0^2\left[-\frac{\mu}{x} + (\mu+1)\,x\right], \tag{A6}$$

by introducing a dimensionless mass $\mu = M/M_0$, where

$$M_0 = \frac{\gamma_0}{\gamma_\star\,\mathrm{M}_\odot} \approx 5.6\times10^{10}\,\mathrm{M}_\odot \tag{A7}$$

and a dimensionless radius $x = R/R_0$, where

$$R_0 = \left(\frac{2\,G\,M_0}{\gamma_0\, c^2}\right)^{1/2} \approx 24\,\mathrm{kpc}. \tag{A8}$$

Corresponding scales for velocity and acceleration are

$$V_0 = \left(\frac{G\,M_0}{R_0}\right)^{1/2} = \left(\frac{\gamma_0\, c^2\, R_0}{2}\right)^{1/2} \approx 100\,\mathrm{km\,s^{-1}} \tag{A9}$$

and

$$g_0 = \frac{V_0^2}{R_0} = \frac{G\,M_0}{R_0^2} = \frac{\gamma_0\, c^2}{2} \approx 1.4\times10^{-9}\,\mathrm{cm\,s^{-2}}. \tag{A10}$$

The numerical values given above arise by tuning two parameters of the theory to fit observations, namely R_0 is set to fit the flat rotation curves observed in large spiral galaxies, and M_0 is set to fit the rising rotation curves observed in low surface brightness galaxies (Mannheim 1993, 1997). The mass scale M_0 separates the large spirals ($M > M_0$), in which the source-generated $\gamma_\star$ potential dominates, and the low surface-brightness galaxies ($M < M_0$), in which the cosmology-generated γ_0 term dominates.

The Mannheim potential alters Newtonian dynamics in the outskirts of galaxies. Differentiating the potential gives the inward gravitational acceleration,

$$g = \frac{\mathrm{d}\Phi}{\mathrm{d}R} = g_0\left(\frac{\mu}{x^2} + \mu + 1\right). \tag{A11}$$

The corresponding circular orbit velocity is

$$V = (Rg)^{1/2} = V_0\left[\frac{\mu}{x} + (\mu+1)\,x\right]^{1/2}. \tag{A12}$$

Unlike MOND (Milgrom 1983; Sanders & McGaugh 2002), which is designed to produce flat rotation curves, the Newton–Mannheim potential leads to a rising velocity profile at large R, $V \to V_0(\mu+1)^{1/2}x^{1/2} \propto R^{1/2}$. However, as the Kepler velocity falls, the Mannheim velocity rises, and the velocity gradient vanishes at $x = x_\mathrm{M}$, where

$$x_\mathrm{M} = \left(\frac{\mu}{\mu+1}\right)^{1/2}. \tag{A13}$$

This defines the 'Mannheim radius',

$$R_\mathrm{M} = R_0\left(\frac{M}{M+M_0}\right)^{1/2}, \tag{A14}$$

where the velocity gradient vanishes, and the velocity is

$$V_\mathrm{M} = V_0\left[\frac{\mu}{x_\mathrm{M}} + (\mu+1)x_\mathrm{M}\right]^{1/2} = V_0\,2^{1/2}\,\mu^{1/4}(\mu+1)^{1/4}. \tag{A15}$$

A3 Spherical shells

Spherical shells are the basis functions used to construct more general spherically symmetric mass distributions. By integrating the Newton–Mannheim potential over a spherical shell of mass $M = M_0\,\mu$ and radius $A = R_0\,a$, we find

$$\Phi = V_0^2\begin{cases}\mu\left(-\dfrac{1}{x} + x + \dfrac{a^2}{3\,x}\right) + x & \text{if} \quad x > a,\\ \mu\left(-\dfrac{1}{a} + a + \dfrac{x^2}{3\,a}\right) + x & \text{if} \quad x < a,\end{cases} \tag{A16}$$

where $R = R_0\,x$. The potential is symmetric to an interchange of a and x. In comparison with the point-mass potential (equation A6), the effect of the finite shell size is to reduce the external Newtonian gravity, by a factor of $(1 - a^2/3)$. The potential inside the spherical shell is also non-uniform, so that external shells produce an acceleration towards their centre. We can subtract a constant to make Φ_M vanish at the origin, $\Phi_\mathrm{M} \to \Phi_\mathrm{M} - V_0^2\,\mu\,a$, leaving

$$\Phi = V_0^2\begin{cases}\mu\left(-\dfrac{1}{x} + x - a + \dfrac{a^2}{3\,x}\right) + x & \text{if} \quad x > a,\\ \mu\left(-\dfrac{1}{a} + \dfrac{x^2}{3\,a}\right) + x & \text{if} \quad x < a.\end{cases} \tag{A17}$$

The inward gravitational acceleration is

$$g = \frac{\mathrm{d}\Phi}{\mathrm{d}R} = g_0\begin{cases}\mu\left(\dfrac{1}{x^2} + 1 - \dfrac{a^2}{3\,x^2}\right) + 1 & \text{if} \quad x > a,\\ \mu\left(\dfrac{2\,x}{3\,a}\right) + 1 & \text{if} \quad x < a.\end{cases} \tag{A18}$$

The corresponding circular orbit velocity is

$$V^2 = g\,R = V_0^2\begin{cases}\mu\left(\dfrac{1}{x} + x - \dfrac{a^2}{3\,x}\right) + x & \text{if} \quad x > a,\\ \mu\left(\dfrac{2\,x^2}{3\,a}\right) + x & \text{if} \quad x < a.\end{cases} \tag{A19}$$

Fig. A1 illustrates the effects of the Newton–Mannheim potential. As is well known, the Newtonian potential is constant inside a mass shell. As a result, the inward Newtonian acceleration jumps abruptly to zero as we pass from outside to inside the shell. When we are inside the shell, the Newtonian inverse-square law forces exerted by equal solid angles on opposite sides of the sky have equal magnitude but opposite direction, thus cancelling.

The Mannheim potential likewise makes a transition as we move inside the shell, but in this case the transition is gradual rather than sudden. The far side of the shell has a larger effect than the near side, and thus there is no sudden transition as we move from outside to inside the shell. The interior and exterior terms meet smoothly at $x = a$, effecting a smooth transition between the asymptotic limits $\Phi \to V_0^2\mu\,a$ for $x \ll a$ and $\Phi \to V_0^2(\mu+1)\,x$ for $x \gg a$. Near the centre of the shell we have a harmonic potential, giving Hooke's law acceleration towards the centre of symmetry.

A4 Spherical density profiles

From the results for spherical shells, it is straightforward to construct results for an extended spherically symmetric density profile $\rho(r)$. We define the interior and exterior moments of the mass profile,

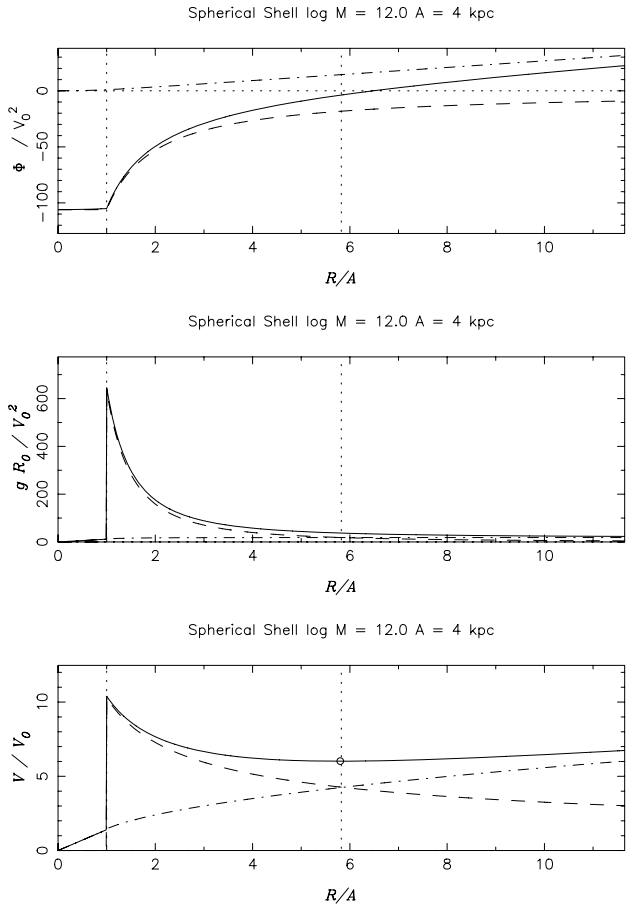

Figure A1. The potential, acceleration, and velocity from a uniform spherical shell. Dashed and dot–dashed curves give results individually for the Newtonian and Mannheim parts of the potential, while the solid curve shows the result when both terms are combined.

$$I_n(R) \equiv \int_{r<R} r^n \mathrm{d}M = 4\pi \int_0^R \rho(r)\, r^{n+2}\, \mathrm{d}r, \tag{A20}$$

$$E_n(R) \equiv \int_{r>R} r^n \mathrm{d}M = 4\pi \int_R^\infty \rho(r)\, r^{n+2}\, \mathrm{d}r. \tag{A21}$$

Here $\mathrm{d}M = 4\pi\rho r^2\, \mathrm{d}r$. Note that $I_0(R)$ is the enclosed mass $M(R)$. In dimensionless form, the moments are $i_n(x) = I_n(R)/M_0\, R_0{}^n$ and $e_n(x) = E_n(R)/M_0 R_0{}^n$, where $x = R/R_0$.

The Newtonian potential,

$$\begin{aligned}\Phi_\mathrm{N} &= -G\left[\frac{I_0(R)}{R} + E_{-1}(R)\right] \\ &= -V_0^2\left[\frac{i_0(x)}{x} + e_{-1}(x)\right],\end{aligned} \tag{A22}$$

depends not only on the interior mass $I_0(R) = M(R)$, which gives rise to the familiar inverse-square law, but also on the exterior moment $E_{-1}(R)$. This exterior moment is usually omitted from the Newtonian potential, and the justification for this omission is somewhat subtle. The inward Newtonian acceleration is

$$\begin{aligned}g_\mathrm{N} = \frac{\mathrm{d}\Phi_\mathrm{N}}{\mathrm{d}R} &= -G\left[\frac{\mathrm{d}}{\mathrm{d}R}\left(\frac{M}{R}\right) + \frac{\mathrm{d}E_{-1}}{\mathrm{d}R}\right] \\ &= \frac{G\,M}{R^2} - \frac{G}{R}\frac{\mathrm{d}M}{\mathrm{d}R} + 4\pi G\,\rho\,R.\end{aligned} \tag{A23}$$

Note that $\mathrm{d}M/\mathrm{d}R = 4\pi R^2\rho$, so that the last two terms cancel – the gradient of $E_{-1}(R)$ is exactly cancelled by the term arising from the gradient of $M(R)$. It turns out that when evaluating gradients of the potential, for both Φ_N and Φ_M, we can treat all of the moments as if they were R-independent constants, even though they are not. This arises because for each term I_nR^k there is a corresponding term E_mR^j, with $n + k = m + j$. The gradient of the first term cancels that of the second term, as mass added to the interior moment balances removal of the same mass from the exterior moment.

Consider next the Mannheim potential

$$\begin{aligned}\Phi_\mathrm{M} &= \frac{\gamma_\star c^2}{2\,\mathrm{M}_\odot}\left(I_0\,R + \frac{I_2}{3\,R} + E_1 + \frac{E_{-1}\,R^2}{3}\right) + \frac{\gamma_0 c^2}{2}R \\ &= V_0^2\left(i_0\,x + \frac{i_2}{3\,x} + e_1 + \frac{e_{-1}\,x^2}{3} + x\right).\end{aligned} \tag{A24}$$

This depends on two interior moments, I_0 and I_2, and two exterior moments, E_1 and E_{-1}. The I_0 term is the linear potential from interior shells treated as point masses at the origin. The I_2 term softens the influence of the interior shells with larger radii. The E_{-1} term represents a harmonic potential arising from exterior shells. The new I_2 and E_{-1} terms arise because the linear potential from the far side is stronger than that from the near side of a shell. The E_1 term has no spatial dependence and hence no physical effect (apart from cancelling the interface term when taking the gradient of I_0R, as discussed above).

Differentiating the Newton–Mannheim potential gives the inward gravitational acceleration,

$$g = g_0\left(\frac{i_0}{x^2} + i_0 - \frac{i_2}{3\,x^2} + \frac{2\,e_{-1}\,x}{3} + 1\right), \tag{A25}$$

and the corresponding circular orbit velocity profile,

$$V = V_0\left(\frac{i_0}{x} + i_0\,x - \frac{i_2}{3\,x} + \frac{2\,e_{-1}\,x^2}{3} + x\right)^{1/2}. \tag{A26}$$

The Newtonian acceleration and Keplerian velocity depend only on the enclosed mass $I_0(R) = M(R)$ and are independent of the exterior moments. The Mannheim acceleration and velocity depend on two interior moments, $I_0(R)$ and $I_2(R)$, and one exterior moment $E_{-1}(R)$.

A5 Hernquist model

The Hernquist model (Hernquist 1990) is a useful approximation to the mass distribution of an elliptical galaxy. It has a finite total mass M, a characteristic radius A, and a density profile

$$\rho = \frac{M\,A}{2\pi\,R\,(R+A)^3} = \frac{M_0}{R_0^3}\frac{\mu\,a}{2\pi\,x\,(x+a)^3}, \tag{A27}$$

where as before the dimensionless variables are $\mu = M/M_0$, $x = R/R_0$ and $a = A/R_0$. Evaluating the required moments, we find

$$i_0 = \frac{\mu\,x^2}{(x+a)^2}, \tag{A28}$$

$$i_2 = \mu\,a^2\left[\frac{x\left(2\,x^2 + 9\,x\,a + 6\,a^2\right)}{a\,(x+a)^2} - 6\,\ln\left(\frac{x+a}{a}\right)\right], \tag{A29}$$

for the interior moments, and

$$e_{-1} = \frac{\mu\,a}{(x+a)^2}, \tag{A30}$$

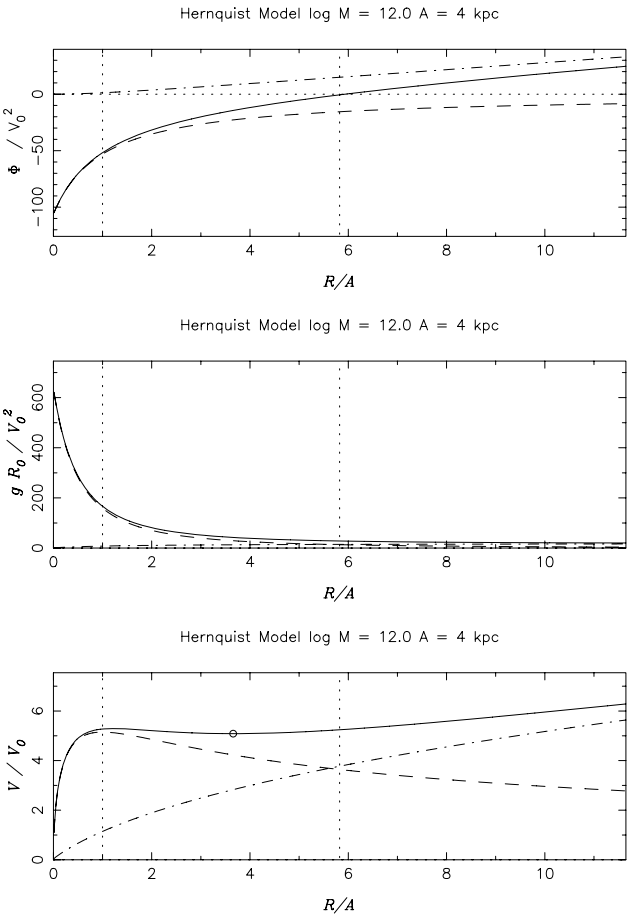

Figure A2. The potential, acceleration and velocity for a spherical model with Hernquist density profile (Hernquist 1990). Dashed and dot–dashed curves give results individually for the Newtonian and Mannheim parts of the potential, while the solid curve shows the result when both terms are combined.

$$e_1 = \mu\, a \left[3 - \frac{a\,(4\,x + 3\,a)}{(x+a)^2} - 2\,\ln\left(\frac{x+a}{a}\right)\right], \tag{A31}$$

for the exterior moments. As in equation (A17), we have added a constant to e_1 so that $\Phi_{\rm M}$ vanishes at the origin.

The inward gravitational acceleration is

$$\frac{g}{g_0} = \frac{\mu}{(x+a)^2} + \mu\left[1 - \frac{2\,a}{x} + \frac{2\,a^2}{x^2}\ln\left(\frac{x+a}{a}\right)\right] + 1. \tag{A32}$$

The corresponding circular orbit velocity is

$$\left(\frac{V}{V_0}\right)^2 = \frac{\mu\,x}{(x+a)^2} + \mu\left[x - 2\,a + \frac{2\,a^2}{x}\ln\left(\frac{x+a}{a}\right)\right] + x. \tag{A33}$$

The first term arises from Newton's inverse-square law, and the other terms arise from Mannheim's linear potential. These results are illustrated in Fig. A2. Note that the velocity remains approximately constant over a wide range in radius and then rises asymptotically as $V \rightarrow V_0\sqrt{(\mu+1)x} = V_0\sqrt{(M+M_0)R/R_0M_0} = \sqrt{G(M+M_0)R/R_0^3}$.

A6 Shielding by an external void

A case of special interest is the uniform density sphere. While such spheres do not exist in astrophysics, a void in which the uniform background baryon density,

$$\bar\rho_{\rm b} = \Omega_{\rm b}\rho_{\rm c}(1+z)^3 = \frac{3H_0^2\Omega_{\rm b}(1+z)^3}{8\pi G}, \tag{A34}$$

is entirely evacuated will act gravitationally like a uniform sphere of negative density $-\bar\rho_{\rm b}$. Since galaxies and clusters of galaxies are assembled by gravitational instabilities that draw material from this initially uniform background, it is reasonable to expect that these mass concentrations are surrounded by voids of comparable mass. Equating the compact object mass M with the mass deficit of the surrounding void, relative to the background density, leads to an estimate of the void radius

$$R_{\rm void} \approx \left(\frac{3\,M}{4\pi\,\bar\rho_{\rm b}}\right)^{1/3} = \left(\frac{2\,G\,M}{H_0^2\,\Omega_{\rm b}}\right)^{1/3}\frac{1}{1+z}. \tag{A35}$$

The effect of an equal-mass void in the background density surrounding each compact mass M is to effectively shield the gravitational effect of that mass from objects at large distances $R \gg R_{\rm void}$. This is somewhat analogous to Debye shielding of charges in a plasma.

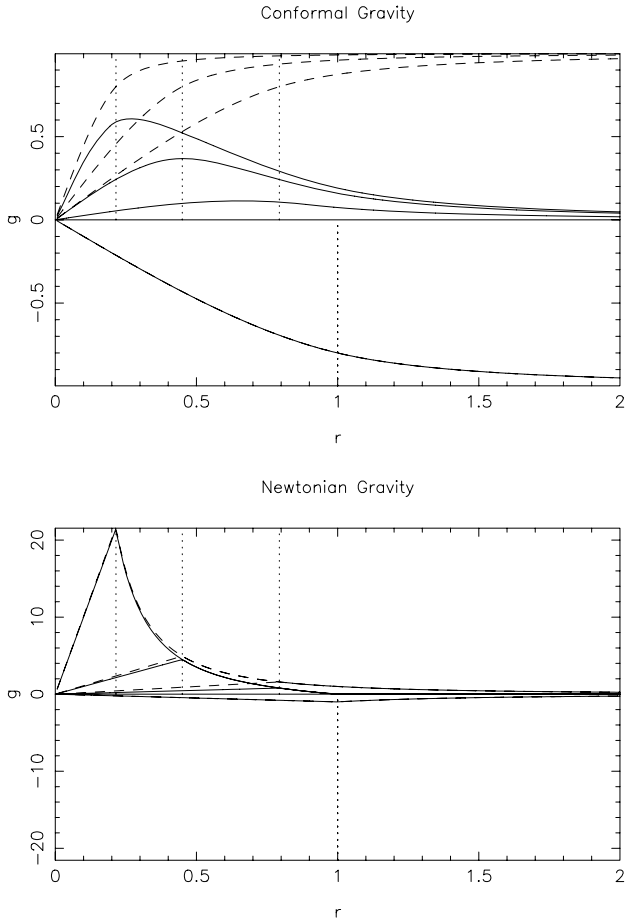

Figure A3. Conformal and Newtonian gravity profiles are shown at three compression ratios for a sphere of matter from a uniform background density that is compressed to a smaller radius. A void in the background density surrounds the compressed sphere, and the negative effective gravity of this void effectively shields long-range gravitational influences of the overdense sphere. Vertical dotted lines give the radii of the void and of the outer edge of the compressed sphere at three overdensities, $\delta = \delta\rho/\bar\rho = 1$, 10 and 100. The dashed lines show the gravity profile from the compressed sphere, the negative curve is the gravity profile from the void, and the positive curves give the inward gravity of the full system.

The Newtonian gravity decreases with radius, and the external effects cancel exactly in spherical symmetry, so that the effect of this shielding is unimportant. In conformal gravity the linear potential $G(M + M_0)\,R/R_0^2$ increases indefinitely with distance R, giving a gravitational acceleration $G(M + M_0)/R_0^2$ that is independent of R. The effective shielding of long-range gravitational influences by the external void around each overdense region is thus essential for practical calculations.

In spherical symmetry the external mass profile also has a gravitational influence, since the linear potential is non-uniform inside a spherical mass shell, giving rise to acceleration towards the centre of the shell. Thus, an external void reduces the effective gravity near its centre by producing an outward acceleration $g(R) \approx GMR/R_0^2 R_{\rm void}$ for $R \ll R_{\rm void}$. Outside the void the acceleration it produces approaches an asymptotic value $g \to G\,M/R_0^2$ for $R \gtrsim R_{\rm void}$.

Thus motivated, we evaluate the gravity at $R = R_0\,x$ for a uniform sphere of mass $M = M_0\,\mu$ and radius $A = R_0\,a$. The dimensionless interior moments are

$$i_n = \begin{cases} \dfrac{3\,\mu\,a^n}{n+3} & \text{if} \quad x > a, \\ \dfrac{3\,\mu\,x^{n+3}}{(n+3)\,a^n} & \text{if} \quad x < a. \end{cases}, \tag{A36}$$

and the dimensionless exterior moments are

$$e_n = \begin{cases} 0 & \text{if} \quad x > a, \\ \dfrac{3\,\mu\,a^n}{n+3}\left[1 - \left(\dfrac{x}{a}\right)^{n+3}\right] & \text{if} \quad x < a. \end{cases} \tag{A37}$$

Inserting these into equation (A25) gives the gravity

$$\frac{g}{g_0} = \begin{cases} \mu\left\{\dfrac{1}{x^2} + \left[1 - \dfrac{1}{5}\left(\dfrac{a}{x}\right)^2\right]\right\} + 1 & \text{if} \quad x > a, \\ \mu\left\{\dfrac{x}{a^3} + \dfrac{x}{a}\left[1 - \dfrac{1}{5}\left(\dfrac{x}{a}\right)^2\right]\right\} + 1 & \text{if} \quad x < a. \end{cases} \tag{A38}$$

The first term in the square bracket arises from Newton's inverse-square law, and the rest of the terms arise in conformal gravity from Mannheim's linear potential.

Fig. A3 illustrates the shielding by the exterior void for the case of a uniform density sphere that is compressed from the uniform density background. At large distances, the inward gravity from the overdensity in the compressed matter is effectively shielded by the negative effective gravity from the mass deficit in the void.

This paper has been typeset from a TEX/LATEX file prepared by the author.